

# Excellently balanced water-intercalation-type heat-storage oxide

Takuya Hatakeyama <sup>1,2</sup>, Norihiko L. Okamoto <sup>1✉</sup>, Satoshi Otake<sup>3</sup>, Hiroaki Sato<sup>3</sup>, Hongyi Li <sup>1</sup> & Tetsu Ichitsubo <sup>1✉</sup>

Importance of heat storage materials has recently been increasing. Although various types of heat storage materials have been reported to date, there are few well-balanced energy storage materials in terms of long lifetime, reversibility, energy density, reasonably fast charge/discharge capability, and treatability. Here we report an interesting discovery that a commonly known substance, birnessite-type layered manganese dioxide with crystal water ( $\delta$ -type  $\text{K}_{0.33}\text{MnO}_2 \cdot n\text{H}_2\text{O}$ ), exhibits a water-intercalation mechanism and can be an excellently balanced heat storage material, from the above views, that can be operated in a solid state with water as a working pair. The volumetric energy density exceeds  $1000 \text{ MJ m}^{-3}$  (at  $n \sim 0.5$ ), which is close to the ideally maximum value and the best among phase-change materials. The driving force for the water intercalation is also validated by the ab initio calculations. The proposed mechanism would provide an optimal solution for a heat-storage strategy towards low-grade waste-heat applications.

<sup>1</sup>Institute for Materials Research, Tohoku University, 2-1-1 Katahira, Aoba-ku, Sendai 980-8577, Japan. <sup>2</sup>Graduate School of Engineering, Tohoku University 6-6-01 Aoba, Aramaki, Aoba-ku, Sendai 980-8579, Japan. <sup>3</sup>Rigaku Corporation, 3-9-12 Matsubara-cho, Akishima, Tokyo 196-8666, Japan.  
✉email: [nlokamoto@tohoku.ac.jp](mailto:nlokamoto@tohoku.ac.jp); [tichi@imr.tohoku.ac.jp](mailto:tichi@imr.tohoku.ac.jp)

The increased demand for energy has strongly called for innovative developments of highly efficient solar cells, excellent high energy-density rechargeable batteries, thermal heat storage devices, etc. The significance of heat storage<sup>1–10</sup> has been increasing in terms of the efficient utilization of low-grade waste heat, because about 60–70% of waste heat is discharged as the heat between 100 and 200 °C<sup>11</sup>. In general, heat storage materials fall into three categories, the sensible heat storage, the latent heat storage via phase-change mechanism regardless of the presence/absence of working pairs, and the thermochemical heat storage including chemical reaction. Desired functions for heat storage materials are high volumetric or gravimetric energy density, high cyclability, no pyrolysis, the feasibility of low-temperature charge to utilize low-grade waste heat, small hysteresis, fast reaction rate, fast reactant transport, heat conduction, fast water penetration in case of using water, etc.

Although lots of studies and review papers have reported many heat storage materials belonging to the above-mentioned categories<sup>10,12–17</sup>, there are few well-balanced materials that combine the energy density, cyclability, fast charge/discharge rate. For example, heat storage materials inevitably must possess a strong environmental resistance. When deliquescence occurs, mass transfer cannot proceed due to inactive coating by the solvent, which causes ill cyclability. Moreover, even if the energy density is excellently high, a low reaction rate and reversibility come to be problematic issues, for example, in the cases of MgO/H<sub>2</sub>O (irreversible reaction)<sup>1,4,18–21</sup>, MgSO<sub>4</sub>/H<sub>2</sub>O (amorphization)<sup>22,23</sup>, CaO/H<sub>2</sub>O (particle fragmentation)<sup>24</sup>, CaCl<sub>2</sub>/H<sub>2</sub>O (e.g., liquefaction, significant degradation of mass transfer)<sup>2,25</sup>, etc. Especially, in MgSO<sub>4</sub>/H<sub>2</sub>O system, sluggish hydration kinetics hinders reversible charge/discharge process; sometimes amorphization is induced upon the dehydration process. Thus, the nonequilibrium phase should not appear if the system completely follows the equilibrium process<sup>26</sup> but this is not the case, which means that the reversible reaction for heat storage is difficult to occur actually in ambient conditions.

Since deliquescence or liquefaction seems a disadvantageous characteristic for heat storage materials, solid-state reaction is preferred for cyclability. In this case, however, the strain effect becomes a key factor. As well as the lithium-ion batteries (LIBs) or rechargeable magnesium batteries, the stress effects cannot be ignored for the materials that can highly accommodate carrier ions<sup>27–33</sup> (in this case molecules), which is well known to retard markedly the battery reaction process. This is a general common problem for the ion/molecule insertion materials. For example, according to Steiger et al.<sup>23</sup>, it has been shown that hydration of MgSO<sub>4</sub>·H<sub>2</sub>O to form MgSO<sub>4</sub>·6H<sub>2</sub>O is a true solid-state reaction until its deliquescence, but its kinetics is strongly hindered due to the strain generation. Thus, the significant strain energy induced by the ion/molecule insertion sometimes exceeds the chemical driving force of the insertion, which retards the kinetic process.

To overcome this situation, allotropic solid-solid phase transformation under pressure (without any working pair) is shown to be useful for application to a heat storage material; a metastably frozen λ-Ti<sub>3</sub>O<sub>5</sub> can transform to β-Ti<sub>3</sub>O<sub>5</sub> under a pressure of 60 MPa, where the latter is the equilibrium phase in ambient conditions and the former phase can be obtained around 460 K and then the metastable λ-phase can be kept even by slow cooling<sup>9</sup>. The enthalpy change related to the phase transformation is about 230 MJ m<sup>-3</sup>, which is about 70% of the melting enthalpy (320 MJ/m<sup>3</sup>) of ice. The entropy change of the transformation is about 25 J K<sup>-1</sup> per mol-Ti<sub>3</sub>O<sub>5</sub>, being comparable to the entropy change (22 J K<sup>-1</sup> per mol-H<sub>2</sub>O) of ice melting. Therefore, the enthalpy change using this mechanism is close to those of phase-change materials (PCMs) using their melting phenomena. Since the heat discharge temperature is tunable by

the application of an external pressure, the external field controlling phase transformation is indeed interesting and deserves to be further investigated.

Nevertheless, to obtain a much larger enthalpy change with the reversible phase transformation towards large heat storage, it is still effective to exploit a large entropy change such as the vaporization entropy change Δ*S*<sub>vap</sub> of water that is about 145 J K<sup>-1</sup> per mol-H<sub>2</sub>O<sup>34</sup>, and this value is found valid also for most of water sorption materials<sup>35</sup>. For the application feasibility of the heat storage materials, as mentioned above, the solid-state reaction should be utilized for storing thermal energy with a working pair H<sub>2</sub>O. To realize this, H<sub>2</sub>O should be inserted into the host material without structural change. In this view, Hatada et al.<sup>1</sup> reported that one mole of La<sub>2</sub>(SO<sub>4</sub>)<sub>3</sub> can accommodate one mole H<sub>2</sub>O while maintaining its original structure, by which rapid and reversible charge and discharge processes can be attained. However, it is necessary to further enlarge volumetric energy density by reducing the large molar volume required for accommodating one mole H<sub>2</sub>O.

It would deserve to note that fast rechargeability and good cyclability are the advantages of the water insertion system compared to others. The best insertion mechanism is believed to be “intercalation” in the narrow sense, as is well-known as the Li insertion mechanism to the layered-rocksalt CoO<sub>2</sub> of LIB system. This is because fewer atoms are needed to store the carrier ions or molecules with little volume change before/after carrier insertion. Here we focus the layered structure of δ-MnO<sub>2</sub> among its polymorphs<sup>36,37</sup>, which is assigned to space group *P*6<sub>3</sub>/*m*mc<sup>38,39</sup>. The interlayer distance of δ-type MnO<sub>2</sub> (~7 Å) is larger than those of the common layered structures such as LiCoO<sub>2</sub> (4.7 Å)<sup>40</sup> and Li<sub>2</sub>MnO<sub>3</sub> (4.7 Å)<sup>41,42</sup>. This is because the δ-MnO<sub>2</sub> structure is stabilized by crystal water molecules and large cations such as K<sup>+</sup> located at interlayers, which is derived from a typical synthesis route (e.g., thermal decomposition of KMnO<sub>4</sub>). It has been reported that the composition is *x* = 0.2–0.3, *n* = 0.5–0.9 in δ-K<sub>*x*</sub>MnO<sub>2</sub>·*n*H<sub>2</sub>O<sup>38,43</sup> and it can allow insertion/extraction of Mg aquo-ion<sup>44–46</sup>. However, it is not clear to what degree thermochemical heat can be absorbed and released, at what rate water can be inserted and extracted, what temperature it can be charged at, i.e., what temperature dehydration occurs. It is also unclear how stable the δ-MnO<sub>2</sub> structure is when the crystal water is lost.

In this work, we demonstrate that δ-K<sub>0.33</sub>MnO<sub>2</sub> possessing a small molar volume (2.78 × 10<sup>-5</sup> m<sup>3</sup> mol<sup>-1</sup>) can accommodate H<sub>2</sub>O up to 0.83 H<sub>2</sub>O per K<sub>0.33</sub>MnO<sub>2</sub> and allow the intercalation of 0.5 H<sub>2</sub>O reversibly around 120 °C at 5 °C min<sup>-1</sup>, whereas charge is feasible below 200 °C even at a very fast rate of 100 °C min<sup>-1</sup>. Thus, a birnessite-type MnO<sub>2</sub> can be an excellently balanced heat storage material that combines a high energy density (~1000 MJ m<sup>-3</sup>), good reversibility with a small hysteresis of about 40 K, fast charge/discharge properties, strong environmental resistance, etc.

## Results

**Thermal analyses under dry or moisture condition.** The chemical composition of the prepared sample in this study was determined to be δ-K<sub>0.33</sub>MnO<sub>2</sub>·*n*H<sub>2</sub>O by the inductively coupled plasma (ICP) analysis. Also from Supplementary Fig. 1, the K element is found to be homogeneously distributed in powder particles. Figure 1a shows the X-ray diffraction (XRD) profile of the pristine δ-K<sub>0.33</sub>MnO<sub>2</sub>·*n*H<sub>2</sub>O powder sample; the crystal structures viewed along the [110] and [001] directions are also depicted, where the possible locations of K<sup>+</sup> and H<sub>2</sub>O are also indicated. Figure 1b shows the weight change of about 13% in thermogravimetry (TG), which was measured during heating up to 280 °C and then down to 50 °C in dry air (dew point < -70 °C). For the as-synthesized sample (blue curve in TG), the heating

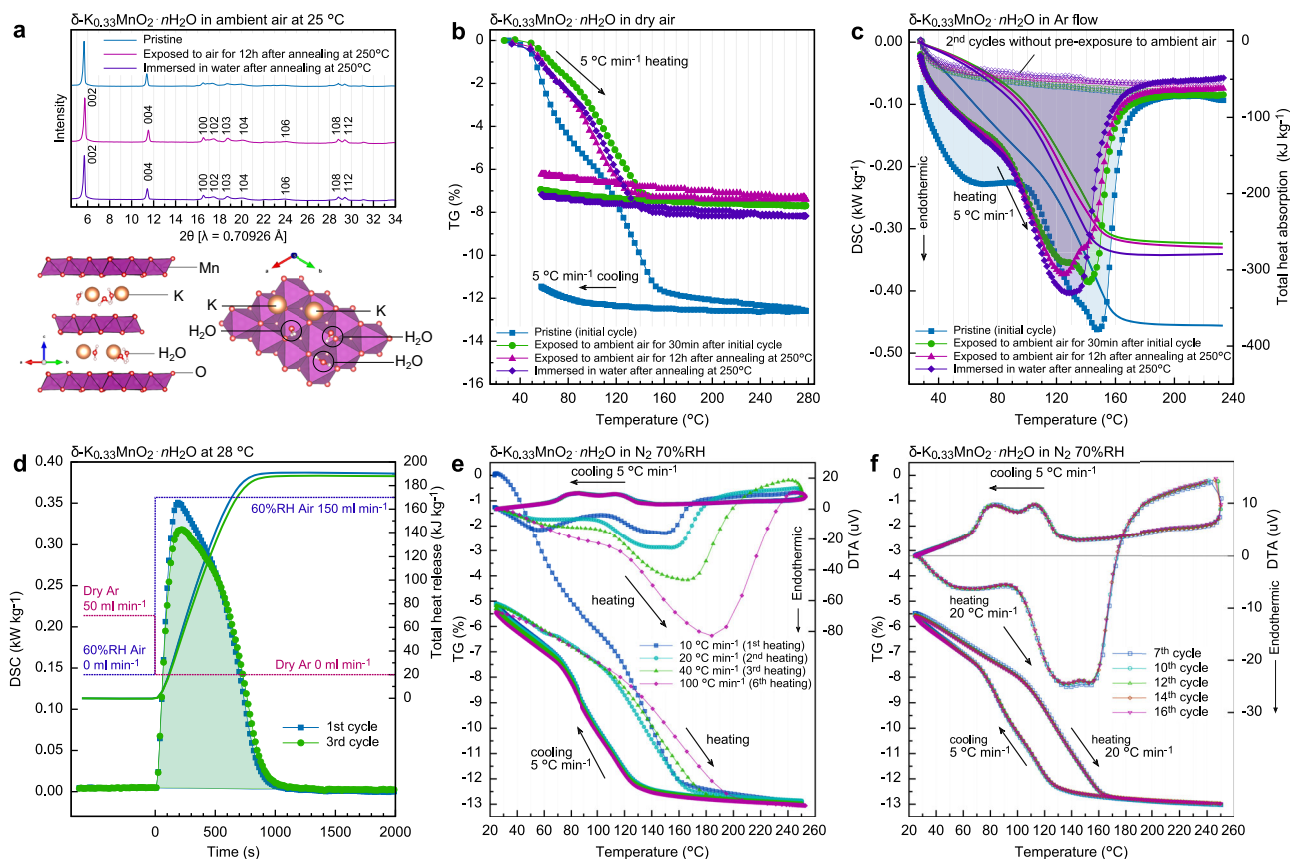


**Fig. 1** Structure and thermal properties of  $\text{K}_{0.33}\text{MnO}_2 \cdot n\text{H}_2\text{O}$ . **a** X-ray diffraction profiles for pristine sample, sample after annealed at 250 °C and then exposed to ambient air for 12 h, and sample after annealed at 250 °C followed by immersion into water. In the lower figure, the layered structure of  $\delta\text{-MnO}_2$  is also shown, where the possible sites for  $\text{K}^+$  and  $\text{H}_2\text{O}$  in space group #194;  $P6_3/mmc$  are indicated in the structure. **b** TG (weight change) profile for samples of (light blue) pristine, (green) exposed to ambient air (60% relative humidity (RH) at 22 °C) for 30 min after initial cycle, (magenta, purple) exposed to ambient air for 12 h or immersed in water after annealed at 250 °C. The reference point (i.e., zero point) in TG is given with respect to the beginning of each TG measurement. **c** DSC profiles during heating (charge). The samples correspond to the respective TG measurements. **d** Isothermal DSC profiles at 28 °C while being exposed to ambient air with 60%RH moisture (discharge). **e** TG-DTA profiles in a  $\text{N}_2$ -gas atmosphere with 70%RH moisture at 25 °C (2.2% $\text{H}_2\text{O}$  in  $\text{N}_2$  gas) at various heating rates (10–100 °C min<sup>-1</sup>). **f** TG-DTA cycle measurement in 2% $\text{H}_2\text{O}$ - $\text{N}_2$  at heating 20 °C min<sup>-1</sup> and at cooling 5 °C min<sup>-1</sup>.

yields a significant weight loss, and the weight hardly recovers upon cooling under the dry condition. However, subsequently, after being exposed to ambient air with moisture (60% relative humidity (RH) at 22 °C) for 30 min (green), the weight decreases again by about 7% (from the sample sufficiently exposed to ambient air) during the second heating, and the weight is substantially unchanged upon the second cooling in dry air as well. That is, about 6% of the weight is lost from the initially synthesized state, but about 7% of weight can reversibly recover in the ambient moisture condition. The same trend in the TG profiles (magenta and purple) is observed also after being exposed to ambient air for 12 h or immersed in water after annealing at 250 °C for 5 h in air; Fig. 1a also shows that the XRD profiles of these samples are very similar to that of the pristine sample, suggesting that the frame structure is almost unchanged after annealing at 250 °C.

Figure 1c shows the heat flow of each sample measured by the differential scanning calorimetry (DSC) apparatus with a heating rate of 5 °C min<sup>-1</sup>. The significantly large endothermic heat is observed during the heating process up to 240 °C, and in the second cycle without exposure to ambient air, such an endothermic heat is not seen for all the samples. The endothermic heat of the pristine sample is 373 kJ per kg-pristine, and after the second cycle, the amount of heat release is 266 kJ per kg-pristine, where “kg-pristine” means the weight of the pristine state “ $\delta\text{-K}_{0.33}\text{MnO}_2 \cdot n\text{H}_2\text{O}$ ” including crystal water. This energy release is

reproducible in cycle treatments, therefore indicating a reversible reaction. Thus, the weight loss and endothermic heat are strongly suggested to be related to the deintercalation of water upon heating. It is noted here that the heat absorption of pristine  $\delta\text{-K}_{0.33}\text{MnO}_2 \cdot n\text{H}_2\text{O}$  (373 kJ kg<sup>-1</sup>) larger than those of the other samples (266–280 kJ kg<sup>-1</sup>) originates from the extra heat absorption at lower temperatures (detected as a shoulder in the DSC profile between 40 and 80 °C), suggesting that the excess water was confined in pristine  $\delta\text{-K}_{0.33}\text{MnO}_2 \cdot n\text{H}_2\text{O}$  during the synthesis process.

Figure 1d shows an isothermal heat release profile measured at 28 °C for dried  $\delta\text{-K}_{0.33}\text{MnO}_2$ . Pristine  $\delta\text{-K}_{0.33}\text{MnO}_2 \cdot n\text{H}_2\text{O}$  was dried by heating up to 240 °C under an Ar atmosphere (charge) and then exposed to humid ambient 60%RH air at 28 °C (discharge); the exposure to humid air rapidly caused an exothermic reaction of dried  $\delta\text{-K}_{0.33}\text{MnO}_2$ . The exothermic heat amounts to 190 and 188 kJ kg<sup>-1</sup> in the first and third cycles, respectively, within about 1000 s, suggesting the high reversibility and reasonable rate capability of heat release.

To make sure whether the water intercalation indeed occurs in the ordinary time scale, we have performed the TG-DTA (differential thermal analysis) measurements in a humidity of 70%RH at 25 °C (atmosphere of 2.2%  $\text{H}_2\text{O}$ - $\text{N}_2$  gas) flow at various heating rates from 10 to 100 °C min<sup>-1</sup> and fixed cooling

rate of  $5\text{ }^{\circ}\text{C min}^{-1}$  by using Thermo plus EVO2 TG-DTA8122/HUM-1 (Rigaku). As shown in Fig. 1e, under this moisture atmosphere condition, the weight loss is completely compensated upon cooling below  $120\text{ }^{\circ}\text{C}$  and finally revert to the original weight on and after the second cycle. Moreover, the DTA profile (temperature difference) corresponds to the TG profile in each cycle; the sample temperature decreases when the sample weight decreases and vice versa. This indicates that the endothermic reaction occurs when the  $\text{H}_2\text{O}$  molecules absorbed in the crystal are liberated, and the exothermic reaction appears when water is inserted into the crystal below  $120\text{ }^{\circ}\text{C}$ . Thus, a series of the reactions are on hydration and dehydration process from the viewpoint of the TG-DTA analysis. Given that a state of about 13% loss in weight around  $260\text{ }^{\circ}\text{C}$  can be regarded as just  $\text{K}_{0.33}\text{MnO}_2$  (i.e.,  $n=0$ ), the pristine state is  $n=0.83$  in  $\delta\text{-K}_{0.33}\text{MnO}_2 \cdot n\text{H}_2\text{O}$  ( $114.84\text{ g mol}^{-1}$ ), and the hydrated state before the weight loss of about 7.8% in the second cycle corresponds to  $n=0.50$  ( $108.76\text{ g mol}^{-1}$ ). Consequently, the stored energy is  $42.9\text{ kJ per mol-K}_{0.33}\text{MnO}_2$  for  $n=0.83$ , and  $30.5\text{ kJ per mol-K}_{0.33}\text{MnO}_2$  for  $n=0.50$ , which means that  $51.9\text{ kJ per mol-H}_2\text{O}$  (derived from the former) and  $61.7\text{ kJ per mol-H}_2\text{O}$  (from the latter). The released heat shown in Fig. 1d amounts to  $21.82\text{ kJ per mol-K}_{0.33}\text{MnO}_2$  for  $n=0.50$ , corresponding to  $44.07\text{ kJ per mol-H}_2\text{O}$ . These differences are discussed later.

Furthermore, as to the kinetics of hydration and dehydration, even when heating at  $100\text{ }^{\circ}\text{C min}^{-1}$ , the dehydration completes around  $190\text{--}200\text{ }^{\circ}\text{C}$ , which is slightly higher than the relevant temperature ( $160\text{ }^{\circ}\text{C}$ ) at a heating rate of  $10\text{ }^{\circ}\text{C min}^{-1}$ . Thus, this small difference of only  $30\text{ }^{\circ}\text{C}$  in the dehydration-completion temperature means that the  $\text{H}_2\text{O}$  diffusion in the crystal is quite rapid. Figure 1f shows completely the same TG-DTA profile of each cycle, indicating very good reversibility of the hydration/dehydration cycle. Note that the slope of TG upon cooling below  $120\text{ }^{\circ}\text{C}$  and that upon heating between  $100$  and  $160\text{ }^{\circ}\text{C}$  are substantially the same. Also as seen in Fig. 1e, although the TG profiles upon heating at  $10$  and  $20\text{ }^{\circ}\text{C min}^{-1}$  are quite different in the low-temperature range because the initial amount of water is different, they are substantially overlapped above  $150\text{ }^{\circ}\text{C}$ . Namely, the same profile as that at  $20\text{ }^{\circ}\text{C min}^{-1}$  is expected to be obtained reasonably also by heating at  $5\text{ }^{\circ}\text{C min}^{-1}$ . These indicate that the heating and cooling rate between  $5$  and  $20\text{ }^{\circ}\text{C min}^{-1}$  substantially would yield little difference in the hydration and dehydration kinetics.

**Structure change under dry or moisture condition.** Actually, how much different is the dehydrated structure from the original structure? Fig. 2a shows the 002 diffraction peak profiles upon heating and cooling processes in ambient conditions ( $60\text{--}80\%$  RH at about  $20\text{--}25\text{ }^{\circ}\text{C}$ ) or under a dry  $\text{N}_2$  gas flow; the 002 diffraction is a characteristic one of  $\delta\text{-K}_{0.33}\text{MnO}_2$  representing the interlayer distance along the  $c$  axis. As shown in Fig. 2b, the lattice constant  $c$  of the pristine sample is  $14.4\text{ \AA}$ , which gradually decreases down to  $13.0\text{ \AA}$  with dehydration by an increase in temperature, and it increases with hydration by a decrease in temperature. The slightly larger lattice constant  $c$  observed in the first heating can be understood from the fact that pristine  $\delta\text{-K}_{0.33}\text{MnO}_2 \cdot n\text{H}_2\text{O}$  ( $n=0.83$ ) contains excess water while  $n$  basically ranges from  $0.5$  to  $0.0$  after the second cycle. In contrast, as seen in Fig. 2c, the lattice constant  $a$  determined from the XRD profile in a wide two-theta range (Supplementary Fig. 2) is almost unchanged during heating and cooling. Moreover, as shown in Fig. 2a, b, upon heating the peak split occurs around  $140\text{ }^{\circ}\text{C}$ , indicating a two-phase region, and then an almost dehydrated phase appears around  $160\text{ }^{\circ}\text{C}$ . Although upon cooling the two phases appear again around  $140\text{ }^{\circ}\text{C}$  as well as upon heating (meaning little

hysteresis), the high-temperature phase can be retained down to  $120\text{ }^{\circ}\text{C}$ . Figure 2d summarizes the fraction of hydrated phase estimated from the XRD intensities, indicating the two-phase region between  $120$  and  $140\text{ }^{\circ}\text{C}$ . Thus, such a small temperature hysteresis would be due to the almost equilibrium condition during the in situ high-temperature XRD measurements (spent for about  $30\text{ min}$  at each temperature). Further interestingly, it deserves to note that the lattice constant  $c$  tends to be influenced by the phase fraction. For example, as seen in Fig. 2b, d, when the fraction of hydrated phase is about  $0.6$  in the second heating process (the red plot at  $120\text{ }^{\circ}\text{C}$ ) the dehydrated phase is significantly strained, whereas the hydrated phase is strained when the fraction is as small as about  $0.2$  in the second cooling process (see the green plot at  $140\text{ }^{\circ}\text{C}$ ). This would be due to the coherent strain effect that is yielded when the layered structure is maintained but the crystal water is included inhomogeneously.

On the other hand, in the condition of a dry  $\text{N}_2$  gas flow, as shown in Fig. 2e–h, the first dehydration process causes a decrease in the interlayer distance, but the 002-diffraction peak is substantially unchanged after dehydration even regardless of temperature increase and decrease; see also Supplementary Fig. 3 for a wide two-theta scan. After being exposed to the ambient air ( $80\%$  RH at  $24\text{ }^{\circ}\text{C}$ ), the interlayer distance reverts closely to the original value, although it does not completely. Namely, this shrinkage of the  $c$  axis (or interlayer distance) is found to be caused by the deintercalation of crystal water to evaporate.

From the above XRD measurements, the lattice constants and mass density of the pristine state and reversibly hydrated state (the initial in the second cycle) can be determined. Since the mass densities of  $\delta\text{-K}_{0.33}\text{MnO}_2 \cdot 0.83\text{H}_2\text{O}$  and  $\delta\text{-K}_{0.33}\text{MnO}_2 \cdot 0.5\text{H}_2\text{O}$  are, respectively, determined to be  $3740\text{ kg m}^{-3}$  and  $3588\text{ kg m}^{-3}$ , the maximum heat storage amounts to  $1395\text{ MJ m}^{-3}$  and the thermal energy reversibly stored is  $1007\text{ MJ m}^{-3}$ . These energy densities of  $\delta\text{-K}_{0.33}\text{MnO}_2$  are indeed excellent among those of commonly known PCMs, which is discussed in the “Discussion” section.

**Water-absorption energy estimated by ab initio calculation.** In order to verify the validity of the hydration energy obtained experimentally, with the aid of the ab initio calculation (VASP package), we have computed the internal energy at zero Kelvin of the  $\delta\text{-K}_{0.33}\text{MnO}_2$  lattice with  $n$  mol of  $\text{H}_2\text{O}$  molecules,  $E(n, T)$  at  $T=0$ , for a supercell  $\delta\text{-K}_4\text{Mn}_{12}\text{O}_{24} \cdot 12n\text{H}_2\text{O}$ . Taking account of the molar formation energy  $\epsilon$  of  $\text{H}_2\text{O}$  molecule and kinetic energy ( $=3RT$ ) of 1-mol water vapor, the heat of hydration  $\Delta H_{\text{hyd}}(n, T)$  is given by  $\Delta H_{\text{hyd}}(n, T) \equiv E(n, T) - [E(0, T) + n\epsilon + 3nRT]$ . The values obtained for  $T=400\text{ K}$  ( $127\text{ }^{\circ}\text{C}$ ) are plotted in Fig. 3a, where it is assumed that  $E(n, T) - E(0, T) - n\epsilon = E(n, 0) - E(0, 0) - n\epsilon$ , and the latter of the equation can be computed. This is considered reasonable as a first approximation. In the fully relaxed condition (red), the hydration energy decreases monotonically with an increase in  $n$ , but the lattice constant of the  $c$  axis comes to be much larger than the experimental one (Supplementary Fig. 4). Then, we have imposed a constraint condition that the lattice constants are fixed so as to equal the experimental values to the calculations. In such a condition (blue), the hydration energy shows a downward convexity like a blue curve. This can explain well the experimental phenomenon that the pristine state has a larger crystal water inside the host structure ( $n=0.83$ ) but only the half quantity ( $n=0.5$ ) can be recovered in the next hydration process. Namely, it would be reasonable to consider that the initial hydrated state can be attained only by the synthesis process.

In the calculated  $n$ -dependence of hydration energy, there is a slight energy hump at  $n=0.167$ , which means that the two-phase region should appear in a low concentration range of water (i.e.,



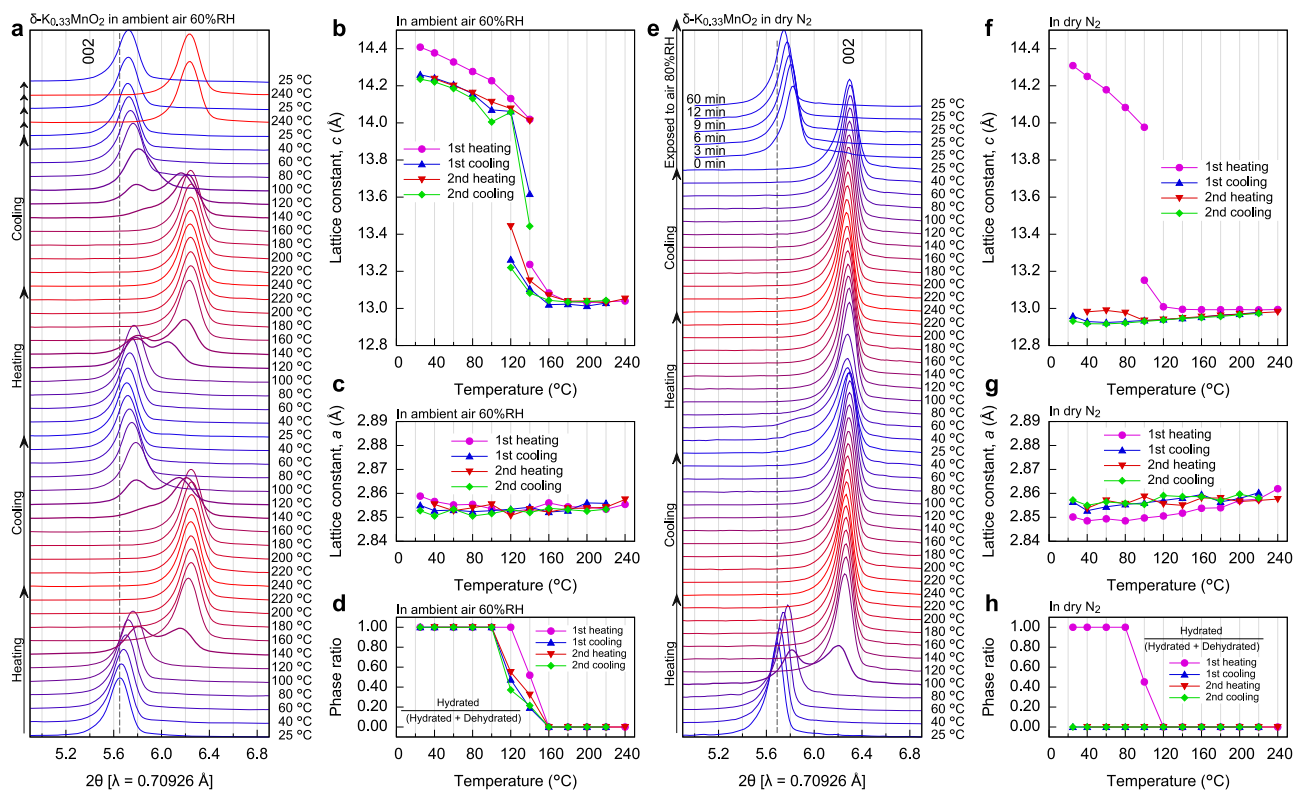


**Fig. 2 Structure changes accompanied by dehydration and hydration cycles.** **a** In situ X-ray diffraction (XRD) profiles for  $\delta\text{-K}_{0.33}\text{MnO}_2$  in an ambient atmosphere (60%RH at 24 °C) for thermal cycle processes between 25 and 240 °C. **b,c** Lattice constants  $c$  (**b**), and  $a$  (**c**) determined from the XRD profiles. **d** Fraction of hydrated phase obtained from the XRD intensities of the hydrated and dehydrated phases. **e-h** In situ X-ray diffraction profiles (**e**), the lattice constants  $c$  (**f**), and  $a$  (**g**), and the phase fraction (**h**) measured under a dry  $\text{N}_2$ -gas flow without moisture. In (**e**), the sample was exposed to an ambient air of 80%RH at 24 °C.

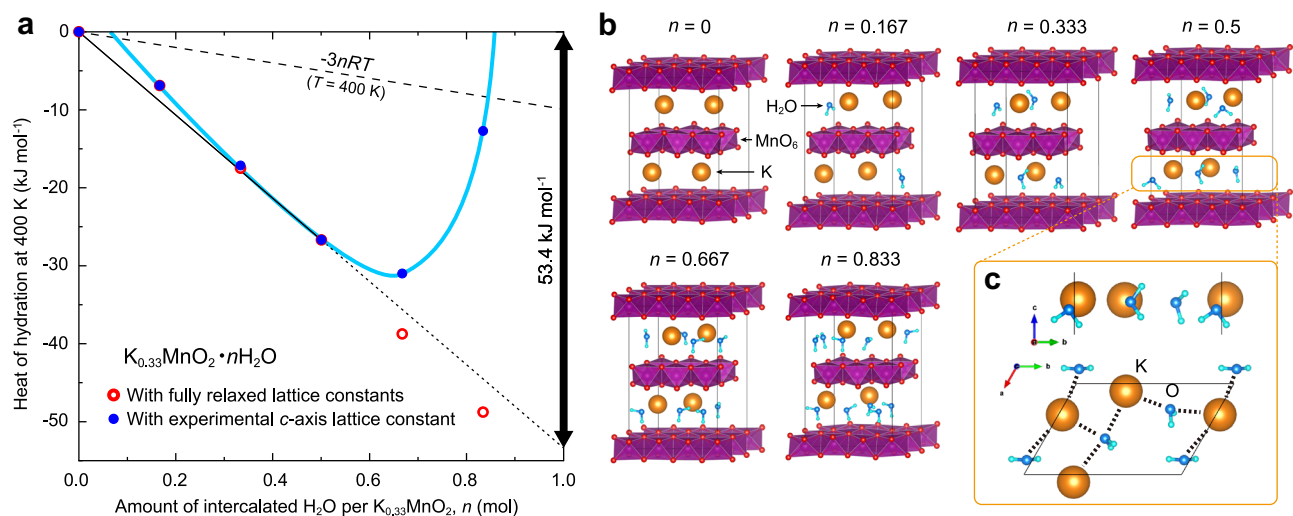


**Fig. 3 Ab initio calculations of hydration heat and optimized structure of  $\delta\text{-K}_{0.33}\text{MnO}_2 \cdot n\text{H}_2\text{O}$ .** **a** Heat of hydration (enthalpy benefit due to the water intercalation) obtained by ab initio calculation for  $\delta\text{-K}_{0.33}\text{MnO}_2 \cdot n\text{H}_2\text{O}$ . **b** The optimized structure with  $\text{H}_2\text{O}$  molecules for each content of water. **c** A typical coordination of  $\text{K}^+$  ions and  $\text{H}_2\text{O}$  molecules sited in an interlayer for  $n = 0.5$ , where the averaged distances of  $\text{K-O}(\text{H}_2\text{O})$  and  $\text{K-H}$  are 2.83 Å and 2.97 Å, respectively. The internal energy of  $\text{H}_2\text{O}$  gas ( $=3nRT$ ) is considered by assuming that  $\text{H}_2\text{O}$  is an ideal gas with degree of freedom 3 (translational) + 3 (rotation). The two sets, free relaxed (red) and fixed lattice constants (blue), are calculated.

at small  $n$ ). Since the TG profile in Fig. 1e has a typical feature of the single-phase reaction, it is difficult to judge what weight in TG the two-phase region appears at. In the light of the XRD results in Fig. 2b, d, since it appears around 140 °C upon heating, which indicates that the two phases coexist in the vicinity of the end of dehydration process upon heating. Therefore, it is concluded that

this ab initio calculation can reproduce well the trend of the present experimental result. What is the most important here is that the heat of hydration  $\Delta H_{\text{hyd}}$  at  $T = 400$  K is estimated to be 53.4 kJ per mol- $\text{H}_2\text{O}$  from the common tangent of the points at  $n = 0$  and at  $n = 0.5$ , which is in fairly good coincidence

with the DSC data (61.7 kJ per mol-H<sub>2</sub>O) obtained for  $\delta$ -K<sub>0.33</sub>MnO<sub>2</sub>·0.5H<sub>2</sub>O; see Fig. 1c and the relevant description.

The optimized structures under the given constraint condition are shown in Fig. 3b, c. The initial sites of K<sup>+</sup> ions in the completely dehydrated structure are 2b and in-between sites of 2b and 2c in space group #194 (*P*6<sub>3</sub>/*m**m**c*); see also Supplementary Fig. 5. In contrast, when  $n = 0.167$  or more than the value, K<sup>+</sup> ions and H<sub>2</sub>O molecules are no longer located at the 2b and 2c sites, being consistent with the previous study on the structure analysis of the  $\delta$ -(K)MnO<sub>2</sub> with H<sub>2</sub>O molecules<sup>38</sup>. The inserted water molecules coordinate to the K<sup>+</sup> ions and pull them out of their stable positions in the crystal, resulting in a random structure that would realize the transverse isotropy in the *ab* plane. The trend that the O atom of H<sub>2</sub>O molecule is bound to K<sup>+</sup> ion (Fig. 3c) is in good agreement with the previous report by Chen et al.<sup>47</sup>. Although K<sup>+</sup> ions are randomly distributed (in the present calculation), the attractive interaction between K<sup>+</sup> ions and H<sub>2</sub>O molecules would result in the ice-like (or solid-like) rather than liquid-like in the state of interplane H<sub>2</sub>O molecules, which is suggested from the entropy analysis in the “Discussion” section. This is consistent with the view expected from Raman spectroscopy measurements (Supplementary Fig. 6). The Raman spectra of  $\delta$ -K<sub>0.33</sub>MnO<sub>2</sub> show a new peak at 560 cm<sup>-1</sup> in the hydrated states, whereas the Raman spectrum of  $\delta$ -K<sub>0.06</sub>MnO<sub>2</sub> (after leaching K<sup>+</sup> ions) hardly shows such a peak even by hydration. This suggests that the insertion of water induces a new vibration mode associated with the hydration structure of K<sup>+</sup>. This is also inferred from the orientation of the oxygen atoms of the water molecules toward the K<sup>+</sup> ions, as can be seen in Fig. 3c. In short, a physical picture of the interlayer dissolution of K<sup>+</sup> ions can be drawn. In addition, it is also shown that  $\delta$ -K<sub>0.06</sub>MnO<sub>2</sub> with few K ions is unstable even above 150 °C and dehydration energy is less than that in  $\delta$ -K<sub>0.33</sub>MnO<sub>2</sub> (see also Supplementary Fig. 7), suggesting that the interlayered K<sup>+</sup> ions not only play a role in strongly stabilizing this layered structure but also contribute to the incorporation of H<sub>2</sub>O into the stabilized crystal as a phenomenon of interlayer dissolution of K<sup>+</sup> ions.

## Discussion

Based on the previous reports<sup>1–9</sup> and the present results, Fig. 4 summarizes the volumetric energy density versus temperature plots for various types of heat storage materials. In this figure, the heat storage materials are classified into “sensible heat storage” (dashed line), “phase change materials (PCMs)” (denoted by yellow), “sorption materials” (green and blue), and “chemical reaction” (red). The “phase change materials” usually utilize the allotropic phase transformation (e.g., melting). In “sorption”, there are two types of materials, physisorption (green) and chemisorption (blue), and gas molecules themselves are basically unchanged in the absorption solid. The former maintains the host structure when absorbing gas molecules, whereas the latter causes the structure to change with gas absorption. In “chemical reaction”, the bonding form of gas molecules are broken to be accommodated inside the solid substance while changing its original structure. These features are summarized in the inset table.

Gas-molecule insertion, intercalation, or surface-adsorption materials belong to “physisorption”. Basically, insertion or intercalation materials can absorb gas molecules inside while maintaining the host structure and only utilize the phase transformation between gas and firmly absorbed state in solid (i.e., vaporization); in this sense, the physisorption materials also belong to PCMs. In the first place, in order to store a large thermal energy, it is quite essential to consider how to freeze such a high entropy state down to the operating temperature. In other words, the intercalation-type PCMs using water as a working pair

enable effectively to utilize the high entropy state of water vapor by freezing dry of their dehydrated state of PCMs.

Here let us delve into the intercalation materials, such as  $\delta$ -MnO<sub>2</sub>, that exploit the “water vaporization”. Under constant pressure, since the heat of hydration (enthalpy benefit) is given by  $\Delta H_{\text{hyd}} = T\Delta S_{\text{hyd}}$ , in the case of the present ab initio calculation, given that the reaction temperature is 400 K, the hydration entropy  $\Delta S_{\text{hyd}}$  is inversely evaluated to be 134 J K<sup>-1</sup> per mol-H<sub>2</sub>O. It deserves to note that the hydration entropy  $\Delta S_{\text{hyd}}$  is very close to the vaporization entropy  $\Delta S_{\text{vap}}$  from a solid state ( $\sim 145$  J K<sup>-1</sup> per mol-H<sub>2</sub>O)<sup>35</sup>. Actually, in the case of the present experiment (61.7 kJ per mol-H<sub>2</sub>O), the (de)hydration temperature is estimated to be 425 K (152 °C), which is very close to the experimental value (120–160 °C), as seen in Figs. 1e and 2b. In addition, the isothermal water-intercalation DSC profile (Fig. 1d) allows precise estimation of entropy change. The exothermic heat of 44.07 kJ per mol-H<sub>2</sub>O observed at 28 °C (301 K) indicates the entropy change of 146.4 J K<sup>-1</sup> per mol-H<sub>2</sub>O. The good agreement of this entropy change accompanied by water intercalation with the sublimation entropy of water ( $\sim 145$  J K<sup>-1</sup> per mol-H<sub>2</sub>O) suggests that the water molecules in the interlayer space of  $\delta$ -MnO<sub>2</sub> is ice-like (or solid-like) rather than liquid-like, and this interpretation is in accordance with the previous report by Chen et al.<sup>47</sup>. Thus, the hydration energy (i.e., amount of heat storage with H<sub>2</sub>O as a working pair) is dominated by the vaporization entropy of H<sub>2</sub>O and H<sub>2</sub>O-release temperature. This would be true as far as H<sub>2</sub>O gas is separated out from the absorption substance in the dehydrated state, even if the H<sub>2</sub>O molecules are broken, for example, changed to H/OH inside the substance.

Based on the above argument, consequently, the heat storage due to the enthalpy gain is given by  $\Delta H = T_{\text{charge}}\Delta S_{\text{vap}}$  per one mole of water, where  $\Delta H \geq 54$  kJ per mol-H<sub>2</sub>O is guaranteed if the charge temperature  $T_{\text{charge}} \geq 373$  K. Therefore, although the operating temperature of heat storage materials may frequently be room temperature, it would be preferred that the charge temperature  $T_{\text{charge}}$  (i.e., H<sub>2</sub>O-release temperature) is as high as possible in terms of a large capacity of thermal energy storage. Nevertheless, from the practical point of view, a possible charge temperature is in the range of low-grade waste heat (373 K  $\sim$  473 K)<sup>11</sup>. Thus, the upper limit of the heat storage can be estimated to be  $\Delta H \sim 69$  kJ per mol-H<sub>2</sub>O (at 473 K) for the water-intercalation-type heat storage materials. If larger heat storage materials are demanded, we have to choose “chemisorption” or “chemical reaction” materials. However, since both heat storage materials cannot absorb gas molecules while maintaining their host structure, the reversibility comes to worse in general. Especially, in “chemical reaction” materials, the charge temperature  $T_{\text{charge}} (= \Delta H / \Delta S_{\text{vap}})$  inevitably becomes higher (over the low-grade waste heat level) due to the compensation of large  $\Delta H$ .

It is necessary for increasing the volumetric heat-storage capacity to reduce the molar volume or number of atoms required for accommodating one molecule of H<sub>2</sub>O. Therefore, what we have to discuss for intercalation materials is how much volume of the host material is required for the H<sub>2</sub>O accommodation. Focusing on the difference between chemisorption and physisorption materials, let us infer the volume needed for hosting one mole H<sub>2</sub>O without any structure change. As suggested by blue-circle data in Fig. 4, it would be reasonable to consider that the upper limit of the ratio of “number of atoms in guest” to “number of atoms in host” would be 1/1 (the figure in the parentheses); for example, CaSO<sub>4</sub>/2H<sub>2</sub>O (1/1), as well as Na<sub>2</sub>S/5H<sub>2</sub>O (1/5) with the guest-host atom number ratio of unity or higher, cannot maintain the host structure with H<sub>2</sub>O absorption as depicted in the inset. Thus, under the constraint case where H<sub>2</sub>O can be stored without any change of the host structure, the maximum amount of H<sub>2</sub>O accommodation would be empirically 1/1 in the atom-number ratio like MnO<sub>2</sub>/H<sub>2</sub>O.

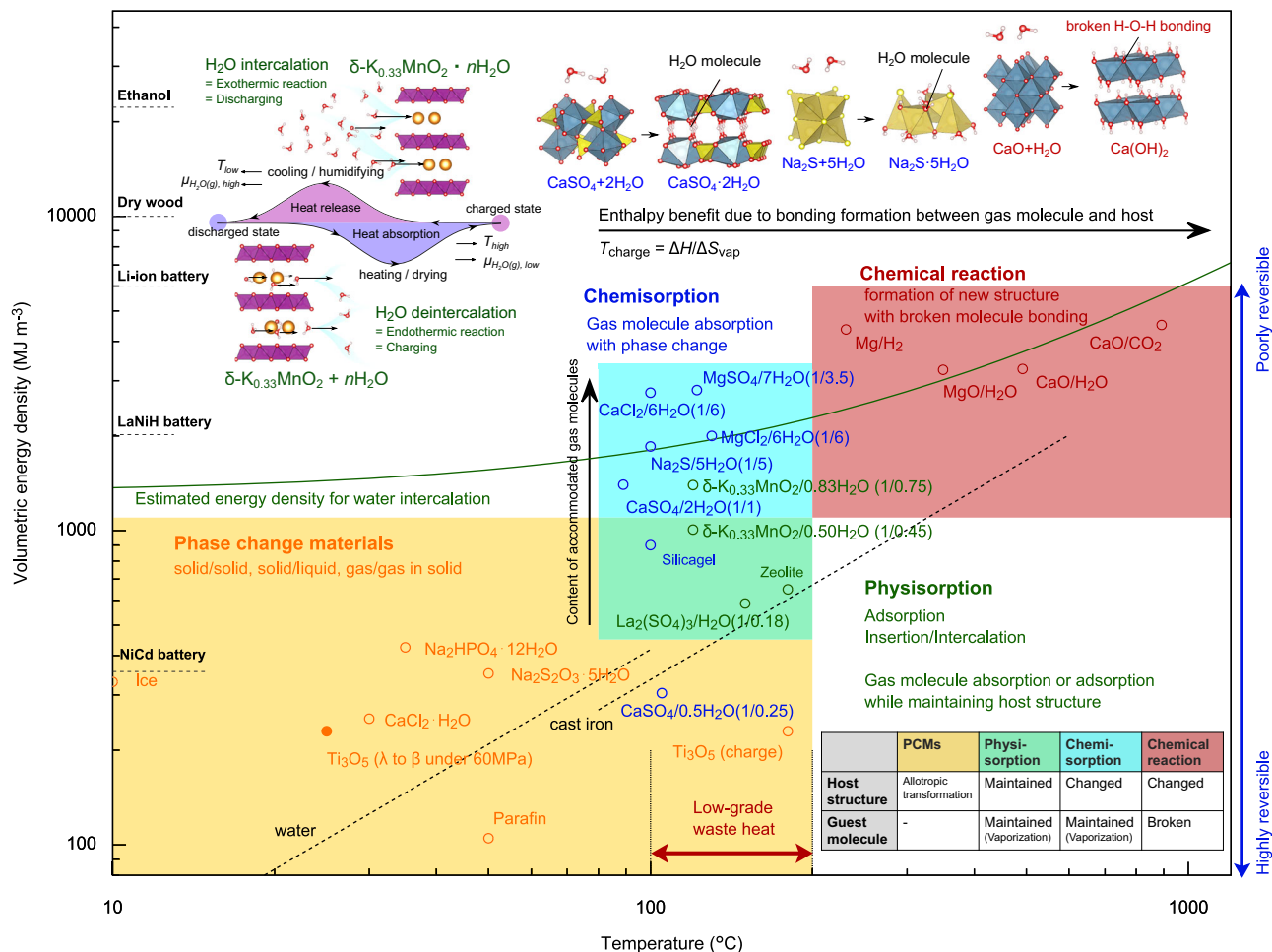


**Fig. 4 Volumetric energy density versus temperature plots for various types of heat storage materials.** The data other than the present data are taken from the references<sup>1-9</sup>. The heat storage materials represented by blue and red change the initial host structure when accommodating gas molecules, where gas molecules are kept inside heat storage materials in the blue category but the bonding of molecules are broken inside heat storage materials in the red category. In contrast, heat storage materials denoted by green can absorb gas molecules while maintaining the host structure. The figure in parentheses denotes the ratio of “number of atoms in guest” to “number of atoms in host”. The dashed lines are depicted for water (heat capacity 4.18 kJ K<sup>-1</sup> kg<sup>-1</sup>, density 1000 kg m<sup>-3</sup>) and cast iron (0.46 kJ K<sup>-1</sup> kg<sup>-1</sup>, 7280 kg m<sup>-3</sup>) given that the reference temperature is set to 0 °C. The green curve indicates the ideal maximum energy density per dehydrated substance volume (based on the manner presented here) that is estimated for water-intercalation materials.

Here, for the sake of simplicity and versatility, the volume of one mole of atoms is supposed to be 1 × 10<sup>-5</sup> m<sup>3</sup> per mol-atom; see the relevant description in Methods. Then, the volume of the host matrix required for storing one mole of H<sub>2</sub>O is 3 × 10<sup>-5</sup> m<sup>3</sup> per mol-3atoms. Based on this argument, the ideal stored energy density for water-intercalation materials is given by  $\Delta H = (3 \times 10^{-5})^{-1} T \Delta S_{\text{vap}} = 4.833 T \text{ MJ m}^{-3}$ , which is also drawn by the green curve in Fig. 4. Consequently, this gives that the stored energy around 400–473 K is about 1900–2290 MJ m<sup>-3</sup>, which is around an ideally maximum amount of stored enthalpy by using vaporization of water with low-grade-waste heat. Note that the volumetric energy density obtained by this equation corresponds to one based on the unit volume before hydration and actually the nominal value shifts downward. Thus, it is noteworthy to mention that we obtained a very excellent and rationalized value exceeding 1000 MJ m<sup>-3</sup> of the stored heat with 0.5 mol-H<sub>2</sub>O per 1-mol δ-(K)MnO<sub>2</sub> in the present discovery. Incidentally, even if H<sub>2</sub> gas or CO<sub>2</sub> (other than H<sub>2</sub>O gas) is a counterpart of working pair, the above idea is substantially applicable because  $\Delta S_{\text{vap}}$  is almost the same (140–145 J K<sup>-1</sup> per mol-gas) for various gases at the temperature where the standard Gibbs formation energy  $\Delta G^{\circ} = 0$  holds; for

example,  $\Delta S_{\text{vap}} = 142 \text{ J K}^{-1}$  per mol-H<sub>2</sub> at 300 °C for Mg + H<sub>2</sub> = MgH<sub>2</sub> and  $\Delta S_{\text{vap}} = 143 \text{ J K}^{-1}$  per mol-CO<sub>2</sub> at 900 °C for CaO + CO<sub>2</sub> = CaCO<sub>3</sub><sup>34</sup>. Why this green curve has deviated toward the lower side in the case of MgH<sub>2</sub> is that H atom is much smaller than the other atoms.

The significance of the present discovery is the demonstration that the mechanism of “water intercalation” in heat storage materials is very advantageous and favorable in terms of their reversibility and reaction rate and, especially, in terms of the best heat storage capacity among PCMs. Furthermore, the layered-structured (K)MnO<sub>2</sub> crystal possesses lots of superiorities for the heat storage materials, in that it is an oxide (not sulfate, sulfide, chloride) that would have the strongest environmental resistance. That is, of course, this material cannot be degraded by environmental oxygen, and can be immersed in water to dissipate heat since it is not dissolved. For the application of heat storage materials, it is crucial to somehow attain a supercooled high entropy state, and freezing dry of δ-K<sub>0.33</sub>MnO<sub>2</sub> after dehydration thermodynamically corresponds to freezing of the water-vapor state that possesses a quite high entropy. Thus, the use of an excellently balanced δ-K<sub>0.33</sub>MnO<sub>2</sub> with moisture/water in an open system would benefit us



towards the application of potential heat storage materials exploiting low-grade waste heat.

## Methods

**Materials preparation and characterization.**  $\delta$ -MnO<sub>2</sub> was prepared following Gaillot et al.<sup>38,39</sup> KMnO<sub>4</sub> (Wako Chemical) crystalline powder was thermally decomposed at 700 °C in air. In order to remove soluble by-products, the powder was washed with distilled water several times until a colorless solution was obtained. The remaining insoluble black powder was filtered and dried in vacuum at 80 °C. ICP optical emission spectrometry confirmed that the composition of the resulting powder was K<sub>0.33</sub>MnO<sub>2</sub>.

X-ray powder diffraction (XRD) analysis was performed using a Rigaku SmartLab diffractometer with MoK $\alpha$  radiation ( $\lambda = 0.70926$  Å). In situ-XRD analysis at controlled temperatures was carried out at a heating rate of 5 °C min<sup>-1</sup> with periods of constant temperature for 30 min to collect diffraction patterns. The samples were placed in ambient air atmosphere (60%RH at 24 °C) or dry N<sub>2</sub> atmosphere during measurement. Crystal structures of MnO<sub>2</sub> polymorphs were visualized with the VESTA program<sup>48</sup>.

For reference, transmission electron microscopy (TEM) observation was also conducted by JEM-2000EXII (JEOL) for as-prepared sample (initially in a sufficiently hydrated state), the results of which are given in Supplementary Fig. 8.

**Thermal analyses under dry or moisture condition.** DSC was carried out using NETZSCH DSC 404 F3 Pegasus for c.a. 10 mg of MnO<sub>2</sub> at a heating rate of 5 °C min<sup>-1</sup> under Ar flow at a rate of 50 ml min<sup>-1</sup>.

Preliminary thermogravimetric analysis under dry air (dew point < -70 °C) was carried out using SHIMADZU DTG-60/60H at a heating rate of 5 °C min<sup>-1</sup>. Thermogravimetric analysis under controlled humidified N<sub>2</sub> atmosphere (70%RH) was performed using Thermo plus EVO2 TG-DTA8122/HUM-1 (Rigaku). The rate capability was measured for the first six cycles at a heating rate of 10, 20, 40, 60, 80, and 100 °C min<sup>-1</sup> whereas the cooling rate was fixed at 5 K min<sup>-1</sup>. Cyclability was subsequently assessed up to 16th cycles at a heating rate of 20 °C min<sup>-1</sup> and a cooling rate of 5 °C min<sup>-1</sup>.

**Ab initio calculation.** The ab initio calculations based on the density functional theory were performed by using the Vienna ab initio simulation package (VASP) code<sup>49,50</sup> with the generalized gradient approximation of Perdew-Burke-Ernzerhof (GGA-PBE) to treat the exchange-correlation functional<sup>51</sup>. A plane wave energy cut-off of 520 eV was used. For structural relaxation and total energy calculations, on-site Coulomb interactions were corrected with the Hubbard *U* parameter of 3.9 eV<sup>52,53</sup>. In order to reproduce the composition of  $\delta$ -K<sub>0.33</sub>MnO<sub>2</sub> with partial occupancy at the K sites, a  $2a_1 \times 3a_2 \times c$  supercell of K<sub>4</sub>Mn<sub>12</sub>O<sub>24</sub> was constructed based on the hexagonal  $\delta$ -Mn<sub>2</sub>O<sub>4</sub> unit cell, followed by appending four K atoms (initially at arbitrary 4 sites of 12 sites in 2c) and an appropriate number of H<sub>2</sub>O molecules (12*n*) in between the MnO<sub>2</sub> slabs. External and internal relaxations were performed under the angle constraint ( $\alpha = \beta = 90^\circ$ ,  $\gamma = 120^\circ$ ) until the energy and forces converged to 10<sup>-6</sup> eV and 5 × 10<sup>-3</sup> eV nm<sup>-1</sup>, respectively. For the total energy calculation of H<sub>2</sub>O, a hexagonal supercell with  $a = c = 15$  Å including one H<sub>2</sub>O molecule was constructed and internal relaxation was performed.

**An estimation of typical atomic volume.** A typical volume of one mole atoms without regard to the atomic species was determined as follows. For example, in the case of Al metal, the molar volume is about 1 × 10<sup>-5</sup> m<sup>3</sup> per mol-Al. Moreover, in the case of  $\delta$ -K<sub>0.33</sub>MnO<sub>2</sub> (99.84 g mol<sup>-1</sup>, 3597 kg m<sup>-3</sup>), the molar volume is 2.78 × 10<sup>-5</sup> m<sup>3</sup> per mol- $\delta$ -K<sub>0.33</sub>MnO<sub>2</sub>, so that dividing by 3.33 atoms gives 0.833 × 10<sup>-5</sup> m<sup>3</sup> per mol-atom, and in the case of water, the reciprocal of 55.6 mol-H<sub>2</sub>O L<sup>-1</sup> (=167 × 10<sup>3</sup> mol-atom m<sup>-3</sup>) gives 0.6 × 10<sup>-5</sup> m<sup>3</sup> per mol-atom. Although the atomic radii of water, metals, and oxides are different, the molar volume of each element is still roughly approximated to be 1 × 10<sup>-5</sup> m<sup>3</sup> per mol-atom, ranging between 0.6 × 10<sup>-5</sup> and 1 × 10<sup>-5</sup> m<sup>3</sup> per mol-atom in the examples.

## Data availability

All the data that support the findings of this study are available within the article and Supplementary Information file, or from the corresponding authors upon request.

Received: 2 October 2021; Accepted: 8 February 2022;

Published online: 17 March 2022

## References

- Hatada, N., Shizume, K. & Uda, T. Discovery of rapid and reversible water insertion in rare earth sulfates: a new process for thermochemical heat storage. *Adv. Mater.* **29**, 1–6 (2017).
- N'Tsoukpoe, K. E. et al. A review on the use of calcium chloride in applied thermal engineering. *Appl. Therm. Eng.* **75**, 513–531 (2015).

- Lee, S. K., Matsuda, H. & Hasatani, M. Fundamental studies of CaSO<sub>4</sub>(1/2) H<sub>2</sub>O/CaSO<sub>4</sub> thermochemical reaction cycle for thermal energy storage by means of chemical reaction. *KAGAKU KOGAKU RONBUNSHU* **12**, 75–82 (1986).
- Mastronardo, E. et al. Strategies for the enhancement of heat storage materials performances for MgO/H<sub>2</sub>O/Mg(OH)<sub>2</sub> thermochemical storage system. *Appl. Therm. Eng.* **120**, 626–634 (2017).
- Paris, J., Falardeau, M. & Villeneuve, C. Thermal storage by latent heat: a viable option for energy conservation in buildings. *Energy Sources* **15**, 85–93 (1993).
- Zondag, H., Kikkert, B., Smeding, S., Boer, Rde & Bakker, M. Prototype thermochemical heat storage with open reactor system. *Appl. Energy* **109**, 360–365 (2013).
- Iyimen-Schwarz, Z. & Lechner, M. D. Energiespeicherung durch chemische reaktionen. I. DSC-messungen zur quantitativen verfolgung der enthalpieänderungen von speicherstoffen für die hin- und rückreaktion (Energy storage through chemical reactions. I. DSC-measurements for enthalpy change following during direct and reverse reactions; in German). *Thermochim. Acta* **68**, 349–361 (1983).
- Hadorn, J.-C. Thermal Energy Storage for Solar and Low Energy Buildings (*The International Energy Agency Solar Heating and Cooling Task 32*, 2005).
- Tokoro, H. et al. External stimulation-controllable heat-storage ceramics. *Nat. Commun.* **6**, 4–8 (2015).
- Pardo, P. et al. A review on high temperature thermochemical heat energy storage. *Renew. Sustain. Energy Rev.* **32**, 591–610 (2014).
- Haddad, C., Périllon, C., Danlos, A., François, M.-X. & Descombes, G. Some efficient solutions to recover low and medium waste heat: competitiveness of the thermoacoustic technology. *Energy Procedia* **50**, 1056–1069 (2014).
- N'Tsoukpoe, K. E., Liu, H., le Pierrès, N. & Luo, L. A review on long-term sorption solar energy storage. *Renew. Sustain. Energy Rev.* **13**, 2385–2396 (2009).
- Jarimi, H. et al. Review on the recent progress of thermochemical materials and processes for solar thermal energy storage and industrial waste heat recovery. *Int. J. Low-Carbon Technol.* **14**, 44–69 (2019).
- Aydin, D., Casey, S. P. & Riffat, S. The latest advancements on thermochemical heat storage systems. *Renew. Sustain. Energy Rev.* **41**, 356–367 (2015).
- Prieto, C., Cooper, P., Fernández, A. I. & Cabeza, L. F. Review of technology: Thermochemical energy storage for concentrated solar power plants. *Renew. Sustain. Energy Rev.* **60**, 909–929 (2016).
- Cot-Gores, J., Castell, A. & Cabeza, L. F. Thermochemical energy storage and conversion: A-state-of-the-art review of the experimental research under practical conditions. *Renew. Sustain. Energy Rev.* **16**, 5207–5224 (2012).
- Yu, N., Wang, R. Z. & Wang, L. W. Sorption thermal storage for solar energy. *Prog. Energy Combust. Sci.* **39**, 489–514 (2013).
- Kato, Y., Yamashita, N., Kobayashi, K. & Yoshizawa, Y. Kinetic study of the hydration of magnesium oxide for a chemical heat pump. *Appl. Therm. Eng.* **16**, 853–862 (1996).
- Kato, Y., Takahashi, R., Sekiguchi, T. & Ryu, J. Study on medium-temperature chemical heat storage using mixed hydroxides. *Int. J. Refrig.* **32**, 661–666 (2009).
- Kato, Y., Nakahata, J. & Yoshizawa, Y. Durability characteristics of the hydration of magnesium oxide under repetitive reaction. *J. Mater. Sci.* **34**, 475–480 (1999).
- Kato, Y., Sasaki, Y. & Yoshizawa, Y. Magnesium oxide/water chemical heat pump to enhance energy utilization of a cogeneration system. *Energy* **30**, 2144–2155 (2005).
- van Essen, V. M. et al. Characterization of MgSO<sub>4</sub> hydrate for thermochemical seasonal heat storage. *J. Sol. Energy Eng.* **131**, 041014 (2009).
- Steiger, M. et al. Hydration of MgSO<sub>4</sub>·H<sub>2</sub>O and generation of stress in porous materials. *Cryst. Growth Des.* **8**, 336–343 (2008).
- Sakellariou, K. G., Karagiannakis, G., Criado, Y. A. & Konstandopoulos, A. G. Calcium oxide based materials for thermochemical heat storage in concentrated solar power plants. *Sol. Energy* **122**, 215–230 (2015).
- Korhammer, K. et al. Sorption and thermal characterization of composite materials based on chlorides for thermal energy storage. *Appl. Energy* **162**, 1462–1472 (2016).
- Vaniman, D. T. et al. Magnesium sulphate salts and the history of water on Mars. *Nature* **431**, 663–665 (2004).
- Ichitsubo, T. et al. Elastically constrained phase-separation dynamics competing with the charge process in the LiFePO<sub>4</sub>/FePO<sub>4</sub> system. *J. Mater. Chem. A* **1**, 2567 (2013).
- Ichitsubo, T. et al. Influence of mechanical strain on the electrochemical lithiation of aluminum-based electrode materials. *J. Electrochem. Soc.* **159**, A14–A17 (2011).
- Kawaguchi, T. et al. Strain-induced stabilization of charged state in Li-rich layered transition metal oxide for lithium ion batteries. *J. Phys. Chem. C* **122**, 19298–19308 (2018).



30. Ichitsubo, T. et al. Mechanical-energy influences to electrochemical phenomena in lithium-ion batteries. *J. Mater. Chem.* **21**, 2701 (2011).
31. Li, H. et al. Circumventing huge volume strain in alloy anodes of lithium batteries. *Nat. Commun.* **11**, 1584 (2020).
32. Shimokawa, K. et al. Structure design of long-life spinel-oxide cathode materials for magnesium rechargeable batteries. *Adv. Mater.* **33**, 2007539 (2021).
33. Shimokawa, K. et al. Zinc-based spinel cathode materials for magnesium rechargeable batteries: toward the reversible spinel-rocksalt transition. *J. Mater. Chem. A* **7**, 12225–12235 (2019).
34. Outokumpu Place of Publication. *HSC Chemistry version 5.1*. (2002).
35. Glasser, L. Thermodynamics of inorganic hydration and of humidity control, with an extensive database of salt hydrate pairs. *J. Chem. Eng. Data* **59**, 526–530 (2014).
36. Hatakeyama, T. et al. Accelerated kinetics revealing metastable pathways of magnesiation-induced transformations in MnO<sub>2</sub> polymorphs. *Chem. Mater.* **33**, 6983–6996 (2021).
37. Hatakeyama, T., Okamoto, N. L. & Ichitsubo, T. Thermal stability of MnO<sub>2</sub> polymorphs. *J. Solid State Chem.* **305**, <https://doi.org/10.1016/j.jssc.2021.122683> (2022).
38. Gaillot, A.-C., Drits, V. A., Plançon, A. & Lanson, B. Structure of synthetic K-rich birnessites obtained by high-temperature decomposition of KMnO<sub>4</sub>. 2. Phase and structural heterogeneities. *Chem. Mater.* **16**, 1890–1905 (2004).
39. Gaillot, A.-C. et al. Structure of synthetic K-rich birnessite obtained by high-temperature decomposition of KMnO<sub>4</sub>. I. Two-layer polytype from 800 °C experiment. *Chem. Mater.* **15**, 4666–4678 (2003).
40. Amatucci, G. G., Tarascon, J. M. & Klein, L. C. CoO<sub>2</sub>, the end member of the Li<sub>x</sub> CoO<sub>2</sub> solid solution. *J. Electrochem. Soc.* **143**, 1114–1123 (1996).
41. Thackeray, M. M. et al. Li<sub>2</sub>MnO<sub>3</sub>-stabilized LiMO<sub>2</sub> (M = Mn, Ni, Co) electrodes for lithium-ion batteries. *J. Mater. Chem.* **17**, 3112 (2007).
42. Strobel, P. & Lambert-Andron, B. Crystallographic and magnetic structure of Li<sub>2</sub>MnO<sub>3</sub>. *J. Solid State Chem.* **75**, 90–98 (1988).
43. Kim, S. H., Kim, S. J. & Oh, S. M. Preparation of layered MnO<sub>2</sub> via thermal decomposition of KMnO<sub>4</sub> and its electrochemical characterizations. *Chem. Mater.* **11**, 557–563 (1999).
44. Nam, K. W. et al. The high performance of crystal water containing manganese birnessite cathodes for magnesium batteries. *Nano Lett.* **15**, 4071–4079 (2015).
45. Kim, S. et al. On the mechanism of crystal water insertion during anomalous spinel-to-birnessite phase transition. *Chem. Mater.* **28**, 5488–5494 (2016).
46. Sun, X., Duffort, V., Mehdi, B. L., Browning, N. D. & Nazar, L. F. Investigation of the mechanism of mg insertion in birnessite in nonaqueous and aqueous rechargeable Mg-Ion batteries. *Chem. Mater.* **28**, 534–542 (2016).
47. Chen, B. R. et al. Understanding crystallization pathways leading to manganese oxide polymorph formation. *Nat. Commun.* **9**, 2553 (2018).
48. Momma, K. & Izumi, F. VESTA 3 for three-dimensional visualization of crystal, volumetric and morphology data. *J. Appl. Crystallogr.* **44**, 1272–1276 (2011).
49. Kresse, G. & Furthmüller, J. Efficient iterative schemes for ab initio total-energy calculations using a plane-wave basis set. *Phys. Rev. B - Condens. Matter Mater. Phys.* **54**, 11169–11186 (1996).
50. Joubert, D. From ultrasoft pseudopotentials to the projector augmented-wave method. *Phys. Rev. B - Condens. Matter Mater. Phys.* **59**, 1758–1775 (1999).
51. Perdew, J. P., Burke, K. & Ernzerhof, M. Generalized gradient approximation made simple. *Phys. Rev. Lett.* **77**, 3865–3868 (1996).
52. Wang, L., Maxisch, T. & Ceder, G. Oxidation energies of transition metal oxides within the GGA+U framework. *Phys. Rev. B - Condens. Matter Mater. Phys.* **73**, 1–6 (2006).
53. Kitchaev, D. A. et al. Energetics of MnO<sub>2</sub> polymorphs in density functional theory. *Phys. Rev. B* **93**, 045132 (2016).

## Acknowledgements

One of the authors, T.I. acknowledges that this work is a derivative study from a series of cathode-material studies for rechargeable magnesium battery, which has been supported by the Advanced Low Carbon Technology Research and Development Program (ALCA-SPRING, grant number: JPMJAL1301) of the Japan Science and Technology Agency (JST). One of the authors, T.H. acknowledges support from Graduate Program in Materials Science at Tohoku University and JST SPRING, Grant Number JPMJSP2114. We gratefully acknowledge the Center for Computational Materials Science, Institute for Materials Research, Tohoku University for the use of MASAMUNE-IMR (Project Nos. 20S0401, 20S0405, and 202012-SCKXX-0401).

## Author contributions

T.I. and N.L.O. conceived the study. T.H., N.L.O., and T.I. designed the research plan and conducted the main part of the experiments, S.O. and H.S. conducted the TG-DTA measurements under the moisture conditions, and partly H.L. made some complementary experiments. N.L.O. conducted the ab initio calculations. Mainly T.I. wrote the manuscript with T.H. and N.L.O. All authors discussed the results and contributed to the manuscript.

## Competing interests

The authors declare no competing interests.

## Additional information


**Supplementary information** The online version contains supplementary material available at <https://doi.org/10.1038/s41467-022-28988-0>.

**Correspondence** and requests for materials should be addressed to Norihiko L. Okamoto or Tetsu Ichitsubo.

**Peer review information** *Nature Communications* thanks Daniil Kitchaev and the other, anonymous, reviewer for their contribution to the peer review of this work.

**Reprints and permission information** is available at <http://www.nature.com/reprints>

**Publisher's note** Springer Nature remains neutral with regard to jurisdictional claims in published maps and institutional affiliations.

 **Open Access** This article is licensed under a Creative Commons Attribution 4.0 International License, which permits use, sharing, adaptation, distribution and reproduction in any medium or format, as long as you give appropriate credit to the original author(s) and the source, provide a link to the Creative Commons license, and indicate if changes were made. The images or other third party material in this article are included in the article's Creative Commons license, unless indicated otherwise in a credit line to the material. If material is not included in the article's Creative Commons license and your intended use is not permitted by statutory regulation or exceeds the permitted use, you will need to obtain permission directly from the copyright holder. To view a copy of this license, visit <http://creativecommons.org/licenses/by/4.0/>.

© The Author(s) 2022